



Article

Effect of Adding Molybdenum on Microstructure, Hardness, and Corrosion Resistance of an AlCoCrFeNiMo_{0.25} High-Entropy Alloy

Mariusz Walczak ¹,* , Wojciech J. Nowak ², Wojciech Okuniewski ¹,* and Dariusz Chocyk ³

- Department of Materials Engineering, Faculty of Mechanical Engineering, Lublin University of Technology, Nadbystrzycka 36D, 20-618 Lublin, Poland
- Faculty of Mechanical Engineering and Aeronautics, Rzeszow University of Technology, Powstanców Warszawy 12, 35-959 Rzeszów, Poland; wjnowak@prz.edu.pl
- Department of Applied Physics, Faculty of Mechanical Engineering, Lublin University of Technology, Nadbystrzycka 36D, 20-618 Lublin, Poland; d.chocyk@pollub.pl
- * Correspondence: m.walczak@pollub.pl (M.W.); wojciech.okuniewski@pollub.edu.pl (W.O.)

Abstract

Recent literature reports have shown that individual HEAs, especially those of the AlCoCr-FeNi composition system alloyed with appropriately selected elements, exhibit excellent mechanical properties and corrosion resistance, making them promising candidates for replacing conventional materials such as austenitic steels in corrosive environments. Therefore, in the present study, the high-entropy alloy AlCoCrFeNiMo_{0.25} was examined and compared with AISI 304L steel and the reference alloy AlCoCrFeNi. The HEA was produced by arc melting in vacuum. The effect of molybdenum addition (5% at.) on the structure, mechanical properties, and corrosion resistance was evaluated. Potentiodynamic polarization and electrochemical impedance spectroscopy tests were carried out in a 3.5% NaCl solution in a three-electrode electrochemical system. The addition of molybdenum to AlCoCrFeNiMox alloy additionally caused, along with the BCC phase, the formation of σ phase and FCC phase (less than 1%), as well as changes in the microstructure, leading to the fragmentation of grains and the formation of a mosaic structure. On the basis of nanoindentation tests, it was established that the addition of Mo increases hardness and elastic modulus and improves nanoindentation coefficients H/E and H^3/E^2 , as well as an increase in the elastic recovery index while decreasing plasticity index (vs. the reference equiatomic HEA). This indicates the improvement of anti-wear properties with impact loading resistance. In turn, electrochemical tests have shown that the addition of Mo improves corrosion resistance. Corrosion pitting develops in Al- and Ni-rich areas of HEA alloys, as a result of galvanic microcorrosion related to Cr chemical segregation. In general, the addition of 5% Mo results in a fine-grained mosaic structure, which primarily translates into favorable nanoindentation and corrosion properties of the AlCoCrFeNiMo_{0.25} alloy.

Keywords: high-entropy alloys; Mo effect; corrosion resistance; nanoindentation

check for updates

Academic Editor: Florina Branzoi

Received: 11 August 2025 Revised: 24 September 2025 Accepted: 28 September 2025 Published: 30 September 2025

Citation: Walczak, M.; Nowak, W.J.; Okuniewski, W.; Chocyk, D. Effect of Adding Molybdenum on Microstructure, Hardness, and Corrosion Resistance of an AlCoCrFeNiMo_{0.25} High-Entropy Alloy. *Materials* **2025**, *18*, 4566. https://doi.org/10.3390/ ma18194566

Copyright: © 2025 by the authors. Licensee MDPI, Basel, Switzerland. This article is an open access article distributed under the terms and conditions of the Creative Commons Attribution (CC BY) license (https://creativecommons.org/licenses/by/4.0/).

1. Introduction

Degradation of materials under various operating conditions, especially in corrosive flow environments, can seriously affect the durability of the components [1]. During use, components are required to withstand various forms of degradation, such as cavitation, abrasive wear, and corrosion. In turn, flow machine components such as pipelines, valves,

Materials 2025, 18, 4566 2 of 22

rotors, and turbines are severely exposed to various forms of deterioration, such as slurry erosion, cavitation, and degradation under corrosive conditions, which intensify their deterioration process [2]. The problems associated with various wear processes require high corrosion resistance from the materials in addition to favorable mechanical properties. Among engineers, stainless steels have so far been the first choice for applications in aggressive corrosive environments [3]. The recent interest in HEAs (high-entropy alloys) may provide an alternative for use in corrosion-resistant steels [4]. Although the corrosion resistance of stainless steels is at an acceptable level, they have relatively limited and sometimes insufficient mechanical properties [5]. Therefore, HEAs with properly selected alloying elements can outperform stainless steels in performance.

The literature describes experiments conducted on hundreds of different alloy compositions with high entropy [6,7]. Not all HEAs exhibit equally good mechanical and corrosion properties. AlCoCrFeNi was one of the first high-entropy alloys studied [8], and interest in this alloy composition is mainly due to its good mechanical properties [9,10]. The properties of this HEA composition can be shaped by changing the molar (or atomic) proportions of the constituent elements that make up the base alloy or by using new additives. The biggest influence on the structure and properties of the Al_xCoCrFeNi alloy is primarily aluminum, where increasing its content in the alloy leads to an increase in strength while decreasing ductility [11]. The increase in aluminum content in the Al_xCoCrFeNi alloy also leads to changes in the structure, i.e., the FCC (face-centered cubic) phase transitions to the BCC (body-centered cubic) phase [12]. Three variants of the structure are then possible, depending on the proportion of x (in molar ratio), i.e., when $x \le 0.4$ there is an FCC phase; a mixed FCC and BCC phase appears between $0.5 \le x \le 0.9$; and when $x \ge 0.9$ a single BCC phase is present [13]. HEA alloy strengthening is associated with network distortion due to the larger size of Al atoms compared to other major alloying elements [14,15].

HEA Al_xCoCrFeNi alloys (like austenitic steels) are also expected to be corrosion resistant due to the content of elements that facilitate the formation of stable passive layers, mainly Cr [16]. As indicated by Shi et al. [17] all common corrosion-resistant alloys, including HEAs, can nevertheless undergo local pitting corrosion. Thus, according to Lin and Tsai [18], the proportion of 0.5 mole of Al in the Al_{0.5}CoCrFeNi alloy leads to the formation of an Al-Ni rich phase (BCC), which is susceptible to galvanic corrosion in a 3.5% NaCl solution. Also, studies of Shi [17] in the alloys for the variants x = 0.5 and x = 0.7 confirmed that pitting is being generated in the BCC structure. In contrast, in the case of single-phase alloys with an FCC structure for x = 0.1 and x = 0.3, pitting rarely forms, and the alloys demonstrate extremely high pitting potential (E_{pit}) and strong corrosion resistance. Also, corrosion tests conducted by Kao et al. [19] in sulfuric acids for options x = 0, 0.25, 0.5, and 1.0 (in molar ratio) revealed that higher Al content determines lower values of pitting potential.

A second solution related to shaping the properties of alloys based on Al-Co-Cr-Fe-Ni composition is the introduction of alloying additives such as Si (reduction in friction coefficient and wear rate) [20], Nb (increase in yield strength and hardness) [21], V (increase in wear resistance) [22], B (better magnetic behavior) [23], Zr (improved mechanical properties) [24], Cu (increase in compressive strength) [25], Ti (increase in hardness and erosion resistance) [26] Mn (improvement of corrosion resistance and solid-solution strengthening) [27], or Mo (improvement of mechanical properties) [28].

For conventional materials such as austenitic steels, the addition of Mo is believed to improve the stability and repassivation abilities of the passive films. This beneficial effect is mainly explained by the fact that Mo modifies the polarity of the passive film by forming of molybdates and preventing Cl^- ingress, rendering the passive film more stable against breakdown [3]. The research of Dai et al. [29] demonstrated that in the case of FeCoCrNiMo_x

Materials 2025, 18, 4566 3 of 22

high-entropy alloys, the addition of Mo enhances the $Cr_2O_3/Cr(OH)_3$ ratio and Mo oxides are incorporated into the passive film. In the case of $Al_{0.5}CoCrFeMo_xNi$ alloy characterized by a mixture of FCC and BCC phases, the addition of Mo enhances formation of the σ phase, which translates into an improvement in hardness and compressive strength of cast alloys and a reduction in ductility of alloys [30]. Unfortunately, too much Mo content is responsible for the formation of the σ phase, which can cause a reduction in corrosion resistance [30,31]. It has been observed that the significant presence of Mo can reduce corrosion resistance due to localized corrosion in areas depleted of Cr and Mo.

Shang et al. [31] pointed out that, in the case of corrosion resistance, it is extremely important to determine the range of Mo content for equiatomic alloys with high entropy, taking into account the best proportion of Mo and σ -phase. As for the available reports related to Mo_x alloying of equiatomic AlCoCrFeNi, only the work of Zhu et al. [28] and one study by the authors [5] are available. Zhu's team studied the effect of Mo on the microstructure and strengthening of alloys. They proved that the addition of Mo increases the strength of the alloy while decreasing its ductility. In contrast, in our earlier paper [5], the characterization of AlCoCrFeNiMo_x alloy (where x = 0, 0.05, 0.1, 0.15, 0.2, 0.25 in molar ratio) in the context of applications in flow environments, including wear sliding and cavitation erosion with limited corrosion characteristics, was presented. Based on preliminary mechanical tests (Vickers hardness and sliding wear) and polarization tests in that study, the Mo0.25 variant showed the greatest application potential in terms of the results obtained. Therefore, it was decided to characterize it more extensively in terms of mechanical properties and corrosion resistance. It should be noted that the Mo0.25 composition is novel in terms of chemical composition and has not yet been studied by other scientists.

This article represents a new approach by the authors in the context of the available literature data, and the current preparation is a broader development of the characterization of AlCoCrFeNi alloy modified with 5% at. Mo, which provides new insights into the structural and mechanical properties based on nanoindentation tests, including corrosion resistance in environments rich in noxious Cl⁻ ion.

2. Materials and Methods

2.1. Materials

High-entropy AlCoCrFeNiMo_x alloys (where x = 0 and 0.25 in molar ratio) were prepared using high-purity (99.99% by weight) Al, Co, Cr, Fe, Ni, and Mo metals as raw materials. The first stage of the work was to weigh each alloy element using a scale with an accuracy of 0.1 mg, so as to obtain the chemical composition given in Table 1. The powders were then mixed in a ball mill for 2 h in an Ar atmosphere (5N purity) to obtain the uniform mixtures of metallic powders. The powder mixtures were cold-pressed in a hydraulic press, molding cylinders with a diameter of 15 mm and a height of about 15 mm. The next stage involved melting cylindrical moldings in an Arc-Melter Edmund Bühler GmbH arc furnace under an argon atmosphere, using a 5-fold remelting of each molding to improve the chemical homogeneity. From the castings prepared in this manner, specimens in the shape of disks with a diameter of 16 mm and a height of 4 mm were cut by wire EDM (ZAP BP 05d, Końskie, Poland). Due to the fact that HEA alloys are an alternative to stainless steel applications, AISI 304L stainless steel was additionally used as a reference material, with the measured chemical composition listed in Table 2.

Materials 2025, 18, 4566 4 of 22

Projected									
Alloy	Al	Co	Cr	Fe	Ni	Mo			
AlCoCrFeNi	20.0	20.0	20.0	20.0	20.0	_			
AlCoCrFeNiMo _{0.25}	19.0	19.0	19.0	19.0	19.0	5.0			
Measured									
Alloy	Al	Co	Cr	Fe	Ni	Mo			
AlCoCrFeNi	18.2	20.2	20.3	20.4	20.8	_			
AlCoCrFeNiMo _{0.25}	18.1	19.3	18.5	19.0	18.7	5.4			

Table 1. Projected and measured chemical composition of investigated HEAs (at. %).

Table 2. Measured chemical composition of AISI 304L stainless steel (wt.%).

С	Mn	Si	P	S	Cr	Ni	N	Fe
0.028	1.541	0.341	0.045	< 0.001	18.23	8.756	0.041	bal.

2.2. Microstructure Analysis

The X-ray diffraction (XRD) pattern was used for phase identification, grain size determination, and stress analysis on the surface of the AlCoCrFeNi and AlCoCrFeNiMo_{0.25} samples. XRD measurements were performed in Bragg–Brentano geometry (θ –2 θ), using a high-resolution diffractometer (Empyrean Panalytical, Almelo, The Netherlands) and recorded using CuK $_{\alpha}$ (l = 1.5418 Å) radiation with K-Beta Ni-filter. The data were collected over the range 2θ = $20 \div 100^{\circ}$ with a step size of 2θ = 0.01 $^{\circ}$ and a counting time of 6 s per data point, using a proportional detector. The fixed divergence slit of $1/4^{\circ}$ was used together with a 5 mm beam mask, and all scans were carried out in a continuous mode. Incident and receiving Soller's slits were 0.04 rad. The crystalline phase in the samples was identified using High Score Plus software v.3.0 package with Crystallography Open Database. XRD patterns of both samples were processed to remove its background noise for peak matching and determining the full-width half-maximum (FWHM) of the corresponding peaks. The Williamsons–Hall plot (W–H plot) method was adopted to calculate the crystallite size of the rich tetragonal σ -phase and its corresponding microstrain in each sample.

The microstructure analysis was performed using a Nova NanoSEM 450 scanning electron microscope (FEI, Eindhoven, The Netherlands) with an EDS detector for elemental composition analysis (EDAX). Observations were made with the GAD detector (gaseous analytical detector, FEI, Eindhoven, The Netherlands). In addition, surface chemical composition analysis (SEM-EDS mapping) was performed on untreated samples using a Phenom ProX scanning electron microscope (Phenom-World, Waltham, MA, USA) with EDS (energy-dispersive X-ray spectroscopy) detector.

2.3. Hardness and Nanoindentation Testing

The hardness was measured on the surface of alloys using a Vickers FM-800 microhardness tester provided with the automatic system ARS 900 (Future-Tech Corp., Kawasaki, Japan). The load used in hardness testing was 9.807 N (HV1) with a dwell time of 15 s. In total, 20 indentations were made for every batch of specimens and the average value of all the measurements was then calculated. The nanohardness of test alloys was measured by the Olivier–Pharr method (Q&P) [32]. Measurements were made in compliance with PN-EN ISO 14577-1 [33] using Anton Paar's Ultra Nano Hardness Tester (UNHT). The surface of the test samples was examined with a Berkovich diamond tip. The load in the test was increased at a steady rate of 20 mN/min from the moment the indenter came

Materials 2025, 18, 4566 5 of 22

into contact with the examined surface until a force $F_{\rm max}$ was reached. For the contact to take place, the following condition had to be met, i.e., the limit rigidity had to exceed 150 μ N/ μ m. The force $F_{\rm max}$ was maintained for 10 s, and then the indenter was unloaded at a steady rate of 20 mN/min. The force F and the indenter penetration depth h were measured. At least 30 tests per every test sample were performed with a force $F_{\rm max}$ of 10 mN. In addition to the standard, most commonly determined mechanical quantities such as H (nanohardness), E (elastic modulus), index H/E (elastic strain to fracture), H^3/E^2 (yield pressure), the elastic recovery index (ERI), and the plasticity index (PI) were also calculated based on the total work performed by the indenter (Equation (1)). The amount of total work performed by the indenter during pressing can be expressed as in Equation (1) below:

$$W_{total} = W_{elast} + W_{nlast} \tag{1}$$

where W_{elast} and W_{plast} represent elastic energy and plastic energy, respectively, determined from the field under the loading–unloading curve of nanoindentation. In turn, the *ERI* and *PI* indicators were determined from Equations (2) and (3):

$$ERI = \frac{W_{elast}}{W_{total}} \tag{2}$$

$$PI = \frac{W_{plast}}{W_{total}} \tag{3}$$

2.4. Corrosion Testing

Electrochemical measurements of the tested materials were carried out in a solution of 3.5% NaCl at ambient temperature (~ 25 °C). The electrochemical properties were tested in a three-electrode system consisting of: a sample as the working electrode, a Pt plate as the counter electrode and a saturated calomel electrode (SCE) as the reference electrode. The Atlas Solich ATLAS 0531 Electrochemical Unit & Impedance Analyzer station was used for electrochemical testing. Measurements of the open circuit potential (OCP) were conducted for 60 min to reach a steady-state potential for all samples.

Electrochemical impedance spectroscopy (EIS) experiments were carried out at OCP from 100 kHz to 100 mHz with an AC amplitude of 5 mV. The results of EIS were determined using AtlasLab software v.2.29 to fit the corresponding equivalent circuit. The polarization curves were recorded with an automatic potential shift of 1 mV/s in the range from -600 mV to +300 mV. The results of the electrochemical measurements were analyzed in AtlasCorr software v.1.04. The values of parameters such as corrosion current density $i_{\rm corr}$ and corrosion potential $E_{\rm corr}$ were estimated from Tafel curves by analyzing potentiodynamic curves in the AtlasLab program. The pitting potential $E_{\rm pit}$ was determined by noting the potential at which a continuous increase in anodic current occurred, indicating sustained localized breakdown of the passive film. The electrochemical measurements were repeated three times to ensure the reproducibility of the result.

On the basis of the current density value i_{corr} , the corrosion rate CR was calculated. The calculation of CR was based on ASTM Standard G 102-89 [34], according to the formula:

$$CR = K \frac{i_{corr}}{\rho} EW \tag{4}$$

where CR—corrosion rate [mm·yr⁻¹], i_{corr} —current density of corrosion [μ A·cm⁻²], K—Reaction rate constant = 3.27×10^{-3} [mm·g· μ A⁻¹·cm⁻¹·yr⁻¹], ρ —density in [g·cm⁻³], and EW—equivalent weight. In addition, the densities of AlCoCrFeN, AlCoCrFeNiMo_{0.25}, and AISI 304L are 7.15 g·cm⁻³, 7.35 g·cm⁻³, and 7.90 g·cm⁻³, respectively.

Materials 2025, 18, 4566 6 of 22

The equivalent weight (EW) values were calculated from the formula:

$$EW = \frac{1}{\sum \frac{n_i \cdot f_i}{M_i}} \tag{5}$$

where

 n_i —valence of the i-th element in the alloy, f_i —mass fraction of the i-th element in the alloy, and M_i —the atomic weight of the i-th element in the alloy.

Calculations of the corrosion rate EW included only those components whose content in the alloy was not less than 1 wt.%. The calculated EW for AlCoCrFeN samples was 18.62, and for AlCoCrFeNiMo_{0.25} samples 18.98. Similarly, EW for AISI 304L is 25.30, which corresponds to the literature data [4].

3. Results and Discussion

3.1. Microstructure Characteristics

X-ray diffraction patterns of AlCoCrFeNi and AlCoCrFeNiMo_{0.25} high-entropy alloy samples are shown in Figure 1. XRD patterns of AlCoCrFeNi showed the diffraction peaks located at around $2\theta = 31.25^{\circ}$, 44.67° , 64.91° , and 82.25° . As a result of analysis using the High Score Plus software v.3.0 package with Crystallography Open Database (COD), it was found that the peak positions in the XRD profiles correspond to phases B2/BCC (COD no. 9008802) with a cubic structure and the space group Pm-3m. The occurrence of a peak at $2\theta = 31.25^{\circ}$ and the absence of peaks around $2\theta = 54.8^{\circ}$ and 72.9° indicate incomplete phase ordering. However, XRD patterns of AlCoCrFeNiMo_{0.25} showed diffraction peaks confirming B2/BCC phases located at around $2\theta = 31.25^{\circ}$, 44.67° , 64.91° , and 82.25° , and new relatively low-intensity peaks at 43.23° and 50.38° representing the FCC phase with a cubic structure and the space group F/m-3m (COD no. 7204808). Additionally, the XRD profile reveals peaks at $20 = 42.16^{\circ}$, 44.61° , 45.67° , 47.93° , 49.29° , and 51.39° , representing the σ-phase with a tetragonal crystal structure and the space group P/42mnm (COD no. 2106167). The above results indicate that adding a small amount of Mo atoms significantly changes the structure of the AlCoCrFeNi high-entropy alloy. The individual phases are marked at the diffraction peaks in Figure 1.

Nair et al. [2] confirmed that the cellular regions of AlCoCrFeNi, which are enriched in Al–Ni and Al–Fe, show B2 ordering. Interestingly, they additionally observed a sigma phase for this alloy variant as well. In contrast, the occurrence of a σ phase in the equivalent AlCoCrFeNi alloy was not confirmed by XRD analysis by Zhu [28], who only found its occurrence with the addition of molybdenum in the amount of Mo0.2. Admittedly, Nair et al. [2] tested an HEA alloy in the form of a shell, while Zhu et al. [28] tested a casting. In contrast, our earlier work [5] did not identify peaks from the FCC phase (around 42.23° and 50.38°), presumably due to limited hardware capabilities from using the Miniflex II X-ray diffractometer made by Rigaku. However, XRD analysis performed with an Empyrean Panalytical high-resolution diffractometer showed the existence of new peaks in the XRD pattern representing the FCC phase, and in this study they are noticeable, although their contribution to the melt is at ~1% level.

The Williamson–Hall method allows us to determine the average grain size and microstrain based on broadening of diffraction peaks in the XRD patterns. This method assumes that the total broadening of the diffraction peaks is a sum of broadening caused by grain refinement and microstrain. The average grain size and macrostrain can be calculated using the Williamson–Hall (W–H) equation:

$$\beta\cos(\theta) = \frac{K\lambda}{D} + 4\sin(\theta)\varepsilon\tag{6}$$

Materials **2025**, 18, 4566 7 of 22

where θ is the diffraction angle, l is the wavelength of X-rays (l=1.5418 Å), K is the Scherer constant, generally taken as 0.9, D is the grain size, and ε is the microstrain. β is the diffraction peak's full-width at half-maximum (FWHM) in radians, corrected by the instrument FWHM. The instrument FWHM was determined using a standard Si reference sample. After measuring β of several diffraction peaks, a curve of β cos(θ) vs. $4\sin(\theta)$ was plotted and fitted linearly by means of the least squares method. The slope of the straight line is the microstrain, and from the intercept of the straight line on the ordinate, the grain size was calculated. Detailed data on the average grain sizes and microstrain of AlCoCrFeNi and AlCoCrFeNiMo_{0.25} samples are summarized in Table 3.

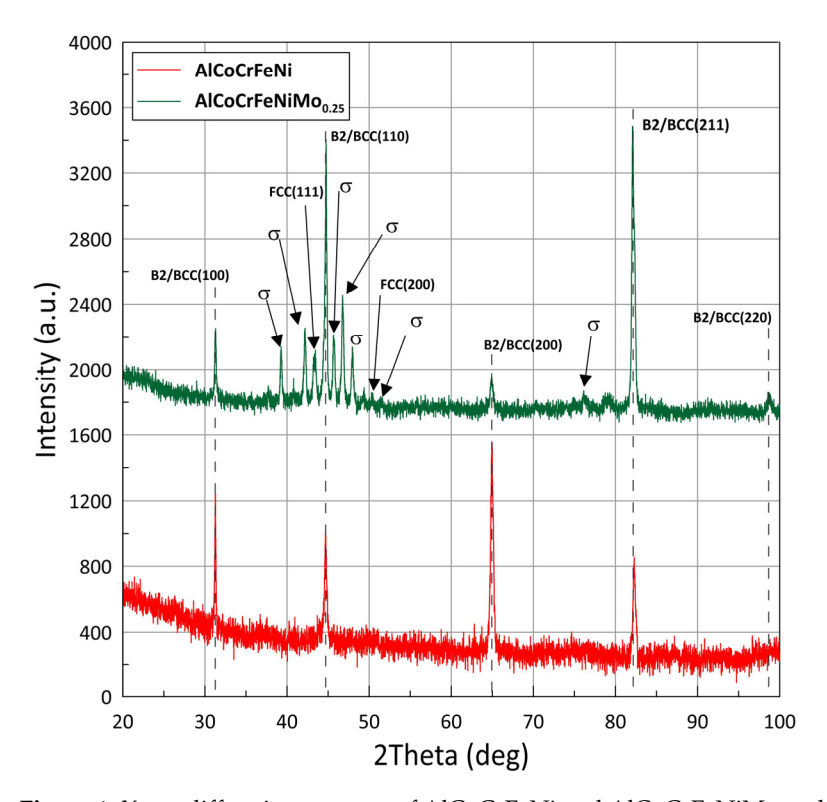


Figure 1. X-ray diffraction patterns of AlCoCrFeNi and AlCoCrFeNiMo_{0.25} high-entropy alloys.

Table 3. The grain size and microstrain.

Sample/Phase	Average Grain Size (nm)	Microstrain (%)
AlCoCrFeNi—B2/BCC	90.69	0.096
AlCoCrFeNiMo _{0.25} —B2/BCC	73.35	0.057
AlCoCrFeNiMo _{0.25} —σ	93.82	0.126

The W–H analysis of the FWHM values of peaks did not show significant microstrain in any phase of the samples. The main influence on peak broadening is the grain size. The analysis shows that the average grain sizes for B2/BCC phases are smaller after Mo addition.

SEM microstructures are shown in Figure 2. The microstructure of the reference HEA samples (Figure 2a) contains both large and small grains, with some grains exhibiting an equiaxed shape. In addition, at higher magnification, it is observed that needle-like phases start to grow beside the grain boundaries, and certain needle-like grains also exist in the centers of the grains (Figure 2c). Similar nucleation of needles at the grain boundaries was demonstrated by Shi et al. [35] for AlFeCrNiMo_{0.8} coatings. EDS analysis of the HEA alloy microspheres (Table 4) showed that the grain boundaries are characterized by a higher

Materials 2025, 18, 4566 8 of 22

concentration of Cr (point B), while the interiors of the grains are dominated by Al (point A). In the case of Mo samples, a structure with much finer grain size was observed (Figure 2b), where, at higher magnification, fragmentation within the grains arranged in a mosaic pattern was observed (Figure 2d). Zhu et al. [28] indicated a similar type of microstructure already observed at Mo0.1 content, describing it as a typical laminar eutectic structure. In addition, in the case of the AlFeCrNiMo_{0.25} alloy, light and dark areas of precipitates were observed in the microstructure. EDS analysis (Table 4) of these sites showed that the darker areas (point A) primarily have higher concentrations of Al and Ni. On the other hand, the brighter ones (point B) have higher proportions of Cr and Mo, with relatively lower concentrations of Al and Ni. As illustrated in Figure 2e, a structure identified as sigma phase separation is displayed. The chemical composition obtained for this phase in the EDS analysis (Table 4, spot C) is similar to the results obtained by Zhu et al. [28] for the sigma phase occurring in the Mo0.2 alloy variant. In contrast to the theoretical thermodynamic information determined using the ThermoCalc program presented in [36], in addition to the typical elements for this phase (i.e., Cr, Fe, Ni, and Mo), EDS analysis (which has its technical limitations), even at high magnifications, indicates elements from the matrix such as Co and small amounts of Al. In the present case, the interlayer distance of the phase was found to be in the range of 100-300 nm. It is important to note that Zhu et al. [28] observed that the interlayer spacing of this phase decrease with increasing Mo content in the alloy.

Table 4. EDS analyses for chemical compositions (at. %) of HEA materials.

Sample	Spot	Phase	Al	Co	Cr	Fe	Ni	Mo
AlCoCrFeNi	A	B2/BCC	20.87	20.17	18.25	19.16	21.55	_
	В	B2/BCC	17.89	19.86	21.57	22.99	22.64	_
	A	B2/BCC	19.27	19.18	18.03	18.41	19.0	5.40
AlCoCrFeNiMo _{0.25}	В	B2/BCC	15.13	20.19	20.62	19.83	17.48	6.75
	C	σ	4.06	19.95	34.75	25.41	7.40	8.44

Figure 2f show the equiaxed coarse microstructure of AISI 304L stainless steel (after electrolytic etching), consisting of austenite with visible twins. The crystal structure of the austenite phase is FCC.

3.2. Mechanical Properties

Surface hardness measurements (Table 5) indicated an increase in average hardness values for all tested HEAs compared to AISI 304L steel. The addition of molybdenum resulted in a more than 3-fold increase in hardness compared to AISI 304L steel and an increase by half compared to the reference HEA alloy without Mo. The resulting increase in hardness for AlCoCrFeNiMo_{0.25} is related to solution hardening and grain size enhancement. Shi et al. [35] indicated that the element Mo, with its large atomic radius, added to the HEA composition causes a strong deformation of the crystal network and, consequently, a significant increase in the strain energy of the crystal network. The obtained Vickers hardness averages for AlCoCrFeNi correspond well with the results obtained by Nair et al. [2], who obtained a value of ~530 HV for this alloy.

Table 5. Surface hardness (HV₁) for different alloys.

Sample	Average Hardness HV_1	SD (–)
AISI 304L	240	± 3.62
AlCoCrFeNi	495	± 17.07
AlCoCrFeNiMo _{0.25}	772	± 27.22

Materials 2025, 18, 4566 9 of 22

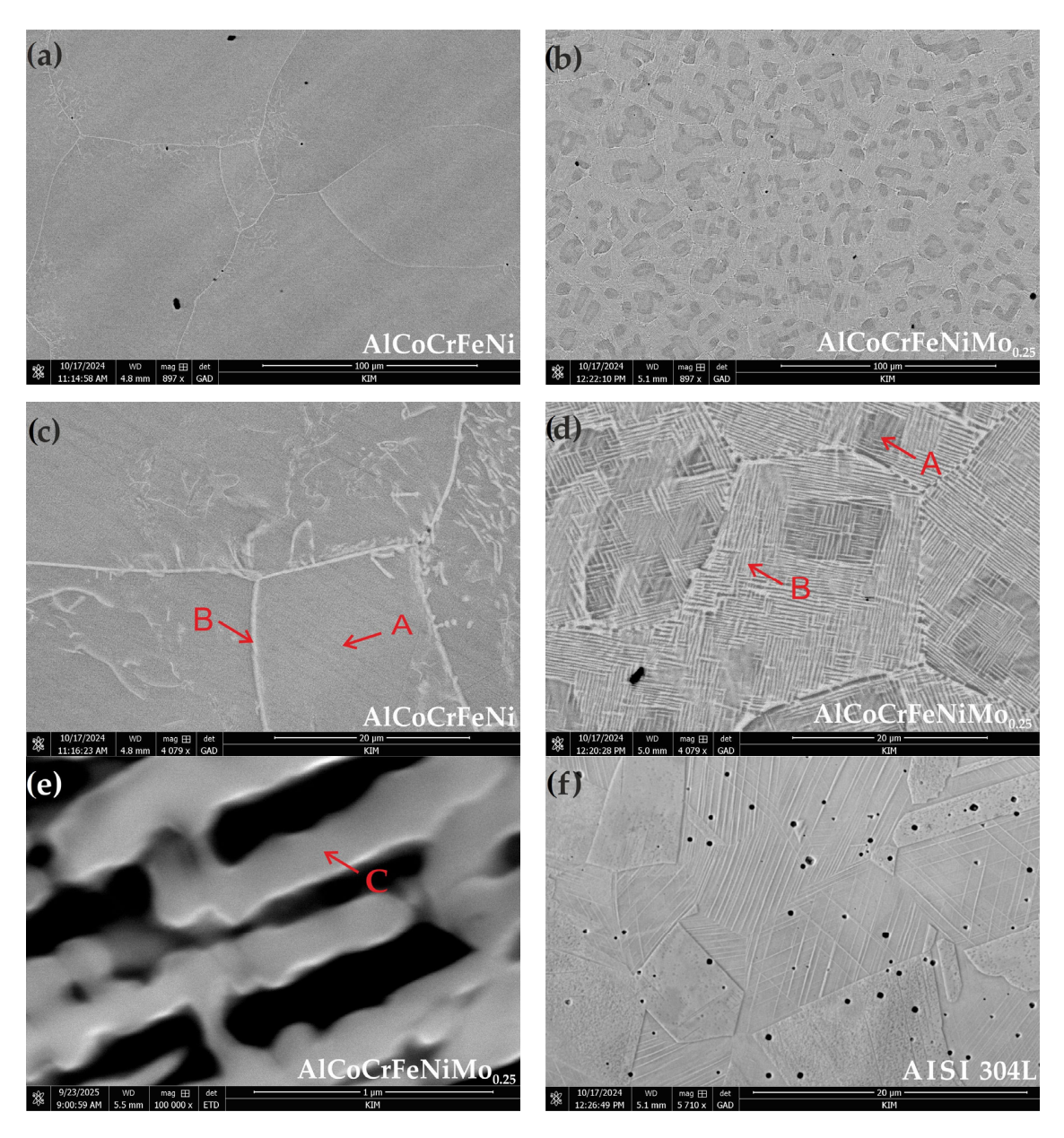


Figure 2. SEM images of the investigated materials with points (A; B and C) of EDS analyses: (a,c)—AlCoCrFeNi (as-cast); (b,d,e)—AlCoCrFeNiMo_{0.25} (as-cast); and (f)—AISI 304L.

The σ phase is unintentionally obtained. As its content increases, the proportion of the BCC phase decreases at the expense of the σ phase. Consequently, the total hardness of the HEA alloy increases, as the hardness of the σ phase is significantly higher than that of the BCC phase. As mentioned earlier, the σ phase is a very hard and brittle intermetallic phase. It increases the hardness of the alloy but reduces its ductility, as has already been demonstrated in studies [28,35].

In our previous studies [5], it was demonstrated that the hardness of the alloy also increases with Mo content, which entails a restructuring of the coarse-grained structure to obtain a fine mosaic-patterned structure. In addition to the presence of the sigma phase, it is primarily the formation of a plate-like structure that contributes to the increase in the phase boundary, which in turn translates into an increase in the strength of HEA alloys with Mo [5,28]. As illustrated (Figure 2 and Table 3), Mo is present in both light and dark plates, with an increased Mo content observed in the lighter plates. The sigma phase occurs in plates with an increased Mo content, i.e., light plates. As Zhu et al. [28] indicated, the strength of HEA material improves significantly with increasing Mo content, while the

Materials **2025**, 18, 4566 10 of 22

ductility of the alloy is weakened. This is due to the fact that the ductility of the sigma phase is lower than that of the BCC phase. Mo occurs in the disordered BCC phase. As a reminder, the atomic radius of Mo is 190 pm, and adding Mo as an element with a larger atomic size can increase the lattice constant of the disordered BCC phase. As a result, its value approaches the lattice constant of the ordered B2 phase. Furthermore, Zhu et al. [28] indicated that the increase in hardness and decrease in ductility of HEA alloys with Mo can be attributed to the fact that the number of slip systems in a complex structure (BCC + σ) is lower than that of a BCC structure. This also explains why the ductility of the σ phase is significantly lower than that of BCC.

Grain refinement in the case of the mosaic structure of the AlCoCrFeNiMo $_{0.25}$ alloy may determine the Hall–Petch effect, contributing to strengthening of the material and increasing its strength [5]. As pointed out by Xu et al. [37], secondary phases influence strain hardening, the strength–ductility balance, and overall mechanical response. Xi and Li [38] indicated that the presence of the σ phase increases alloy strength by anchoring grain boundaries and impeding their movement. This, in turn, prevents the formation of twinning, which reduces ductility. The increase in material strength can also be explained by the effect of σ phase on grain boundaries, blocking both sliding and dislocation motion.

On the other hand, it is difficult to relate the hardness of the AlCoCrFeNiMo_{0.25} alloy to the literature data, since such an alloy composition has not been studied. Figure 3 illustrates the load–displacement curves, and Table 6 summarizes the results obtained from the nanoindentation tests. As can be observed from the curves, at 10 s intervals, all tested materials exhibit a tendency to creep, as the displacement of the diamond indenter increased at a constant maximum load of Fmax = 10 mN. Although creep changes are analyzed at much higher holding times [39], for HEA alloys based on the Al–Co–Cr–Fe–Ni composition, the authors of [40,41] used a holding time of 10 s to determine whether creep occurred. Jiao et al. [41] demonstrated that for an equimolar alloy, a significant accumulation of material around the indenter suggests that strongly localized plastic deformation occurs. In this type of HEA alloy, the deformation mechanism during nanoindentation is explained by an increase in dislocation density, which increases as the indentation depth decreases. The dislocations then spread to smaller slip circles, which can lead to nanoindentation creep.

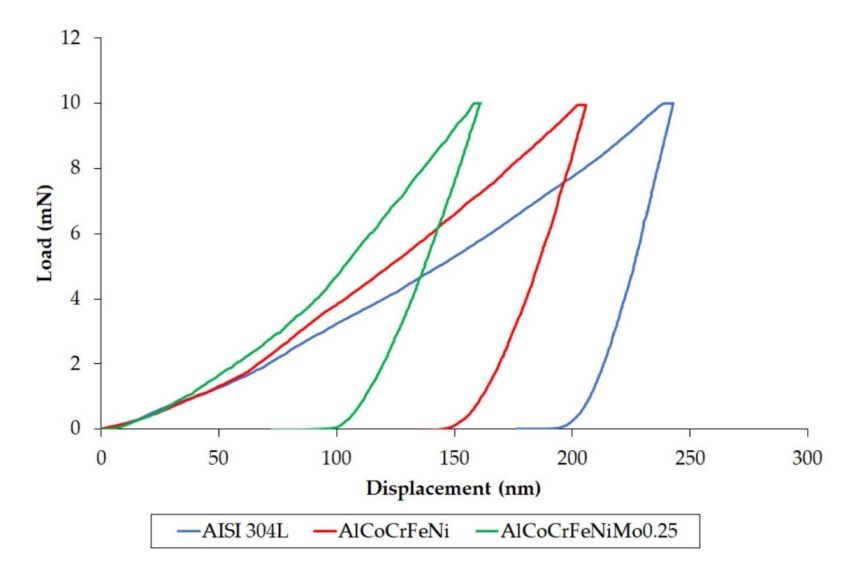


Figure 3. Loading-unloading nanoindentation curves (O&P method) for tested alloys.

Materials **2025**, 18, 4566 11 of 22

Material	H (GPa)	E (GPa)	H/E	H^3/E^2 (×10 ⁻³)	W _{elast} (pJ)	W _{plast} (pJ)	W _{total} (pJ)	Index ERI	Index PI
AISI 304L	5.0 ± 0.4	226.4 ± 24.3	0.022	2.37	180.8 ± 11.2	860.4 ± 31.5	1041.7 ± 31.1	0.17	0.83
AlCoCrFeNi	6.2 ± 0.7	194.4 ± 18.8	0.032	6.51	219.1 ± 6.7	652.8 ± 36.2	871 ± 37.0	0.25	0.75
AlCoCrFeNiMo _{0.25}	13.3 ± 4.1	261.4 ± 35.9	0.050	37.37	252.2 ± 12.4	361.7 ± 99.1	613.8 ± 100	0.41	0.59

Table 6. The mechanical properties of tested materials measured in the nanoindentation test.

On the basis of the load–displacement curves, it is apparent that stainless steel reached the highest maximum depth of penetration, whereas the AlCoCrFeNiMo $_{0.25}$ alloy showed the lowerst. The smaller penetration depth of HEA materials (vs. AISI 304L) is an indication of lower plastic deformation.

For the AlCoCrFeNiMo_{0.25} alloy, a relatively high nanoindentation hardness with a relatively significant standard deviation is recorded (Table 6), which can be associated with the mosaic pattern of the structure and the presence of a σ phase. Molybdenum, which is regarded as a sigmoidal element, also results in higher Young's modulus values. As demonstrated in a study by Zhuang et al. [30], although the formation of the σ-phase can increase the strength of the alloy, it contributes to a decrease in the ductility of the alloy, which consequently contributes to the obtained shares of index ERI and index PI. The index ERI describes the energy dissipated from a sample after the removal of an indentation load and demonstrates the impact loading resistance of an indented sample [42]. On the other hand, the index PI provides information about the mechanical behavior of an indented material during nanoindentation, and it gives the intrinsic plasticity of a material [43]. Analyzing the results for the elastic recovery index, it can be noted that HEA materials dissipated higher energy during nanoindentation measurements, which clearly increases for the alloy with added Mo. At the same time, in addition to stainless steel, it was the reference alloy AlCoCrFeNi that showed the highest plasticity index, which means that it was this alloy (vs. AlCoCrFeNiMo_{0.25}) that undergoes almost the maximum plastic deformation during the nanoindentation test. Based on the results of the plasticity index, it can be concluded that the addition of Mo increased the resistance of HEAs to plastic deformation, probably due the presence of the σ phase. The elastic strain to failure is an indicator of the material's wear resistance, and yield pressure is an indicator of a material's resistance to plastic deformation [44,45]. The higher the H/E index, the more dominant elastic deformation is. Alloys with higher values of H/E tendto show less ductile behavior compared with those featuring lower values [46]. The nanoindentation test suggests that both of these indicators improve after the addition of Mo to the HEA alloy, reaching the highest value. The high wear resistance in the ball-on-disk test for the AlCoCrFeNiMo_{0.25} alloy was confirmed in our earlier work [5].

3.3. Corrosion Behavior

Changes in potential (OCP) over time are presented in Figure 4a. An increase in potential towards higher values indicates the tendency of the material to form a protective passive layer on the surface when reaching a state of equilibrium with the system [47]. Among the materials tested, the highest potential value is achieved by AlCoCrFeNiMo_{0.25}. In turn, the following behave very similarly: AISI 304L and AlCoCrFeNi.

Materials **2025**, 18, 4566

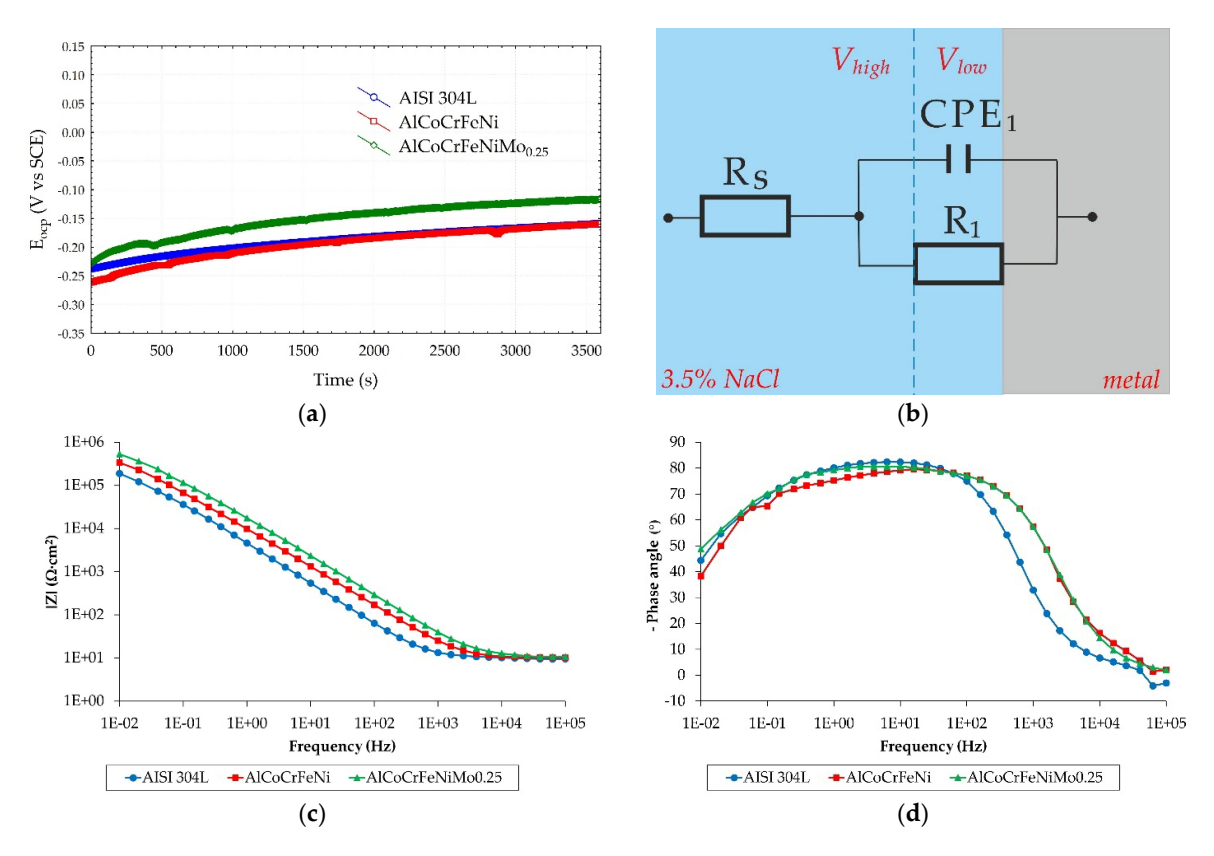


Figure 4. Electrochemical corrosion behavior of tested alloys in 3.5% NaCl solution: (a) open-circuit potential variation with time; (b) schematic of the circuit used for simulating the EIS; (c,d) Bode diagrams.

After the systems reached equilibrium, a non-destructive EIS test was performed. The electrochemical impedance spectrum was simulated using appropriate circuit models to quantitatively determine the resistance and capacity values. Considering the type of electrical equivalent circuit used by Ayyagari et al. [42], and in order to quantitatively determine the polarization resistance values, the EIS data were simulated using a representative circuit shown in Figure 4b, and the determined parameter values were summarized in Table 7. The replacement model consists of a series-connected resistor R_s representing the resistance of the environment (electrolyte) and a parallel arrangement of CPE_1 and R_1 (i.e., a constant phase element and a resistor representing the transition resistance). The EIS method provides additional information about the electrochemical properties of the passive layer of metal alloys [48,49]. For all tested material groups, the environmental resistance (R_s) changes only slightly, which indicates stable measurement conditions and minimal influence of the solution on the variability of results. The polarization resistance (R_1) is important for the assessment of corrosion resistance. In the case of HEA alloys, higher values of the R_1 parameter were observed compared to austenitic steel. A high polarization resistance (R_1) value indicates good corrosion resistance of the tested materials, with the AlCoCrFeNiMo_{0.25} alloy performing best in this comparison.

When analyzing the results for the parameters of the solid-phase element CPE_1 , differences were observed in the value of the coefficient n_1 . Considering the value of the coefficient n_1 , it can be seen that all the tested materials behave almost like an ideal capacitor (according to the dependence $n_1 \rightarrow 1$). This parameter is related to surface heterogeneity. The results of changes in parameter n1 indicate that the surface of the AlCoCrFeNiMo_{0.25} alloy, which is closest to an ideal capacitor ($n_1 = 0.92$), is characterized by a compact passive layer free of defects with very good protective properties, while the passive layer of the

Materials **2025**, 18, 4566

AlCoCrFeNi alloy appears to be the most heterogeneous (values n_1 = 0.88). Additionally, when analyzing the graphical representations of impedance results in the form of a Bode diagram (Figure 4c), it can be seen that the impedance modulus (|Z|) for all analyzed samples exceeded the value of $10^5 \ \Omega \cdot \text{cm}^2$. According to the literature [49,50], fulfilling this relationship for the low-frequency range indicates high corrosion resistance and is characteristic of materials dedicated to medical applications with very high corrosion resistance, such as titanium alloys.

Table 7. Electrical equivalent circuit parameters of EIS spectra.

	R_s R_1		CPE ₁	
Sample No.			Q_{dl1}	
	Ω ·cm ²	$ imes 10^5~\Omega \cdot cm^2$	$ imes 10^{-5}~\Omega^{-1} \cdot S^n \cdot cm^{-2}$	n_1
AISI 304L	9.95	2.57	3.16	0.90
AlCoCrFeNi	10.49	5.01	1.89	0.88
AlCoCrFeNiMo _{0.25}	10.51	6.63	2.09	0.92

 $Q_{\rm dl}$ —constant phase element (CPE_1) of passive film, n—exponent of $Q_{\rm dl}$.

The Bode phase shift diagram (Figure 4d) for the AlCoCrFeNiMo $_{0.25}$ alloy suggests the formation of a stable passive layer on the alloy surface, as the phase angles in the medium-and low-frequency ranges reach their highest values (approximately -80° and -49° , respectively). However, the phase angles for the AlCoCrFeNi alloy drop to approximately -39° at low frequencies, and this behavior indicates that the passive layer forming on the reference HEA alloy contains defects.

The results of the polarization tests in 3.5% NaCl are presented in the form of Tafel curves in Figure 5, and the determined electrochemical parameters are summarized in Table 8. For both HEAs, a favorable shift in the corrosion potential towards higher values relative to stainless steel was observed. However, in the assessment of corrosion resistance, the key parameter is the corrosion current density i_{corr}, which is also correlated with the corrosion rate. In this respect, the AlCoCrFeNiMo_{0.25} alloy performs best among the materials tested. On the other hand, the HEA alloy without Mo performs less favorably than AISI 304L steel. The conclusion from the polarization tests is that it is the addition of Mo to the HEA material that reduces the corrosion current density and improves corrosion resistance compared to the other materials tested. This effect is explained by Dai et al. [29] as the incorporation of MoO_4^{2-} oxides into the passive layer dominated mainly by Cr_2O_3 . The presence of molybdenum oxide in the passive layer of HEA acts as a barrier layer, impeding electrochemical attack. The course of the Tafel curves indicates that all tested materials exhibit a passivation area, after which, in the potential range of $0.12 \div 0.26 V_{SCE}$, the anodic current suddenly increases. This behavior results in local breakdown of the passive film, the formation of corrosion pits, and the determination of the pitting potential E_{pit} corresponding to the transition of current density from constant to rapid increase. The highest E_{pit} value and the most stable and widest passive area are characteristic of AISI 304L stainless steel. The AlCoCrFeNi alloy, in comparison with other materials, showed a gradual and mild increase in current density with observed metastable pitting (at potentials well below E_{pit}), which underwent repassivation. Meghwal et al. [51] indicate that, apart from E_{pit}, faster diffusion of Cl⁻ ions occurs on the alloy surface through defects or corrosion-prone phases, which consequently reduces the protective function of the passivation layer, resulting in local corrosion. In general, in HEAs, the addition of Al has a negative effect on the corrosion resistance of alloys. It has been confirmed that the addition of Al significantly reduces the pitting corrosion potential and increases the pitting corrosion area of these alloys in neutral NaCl solutions [52]. Although the HEA alloy had a higher

Materials 2025, 18, 4566 14 of 22

pitting corrosion potential, the passive area was also smaller than that of stainless steel. The fact that AISI 304 stainless steel exhibits a larger passivation area than the HEA alloys compared to it is not unique, as shown in another study [4], where the AlCu_{0.5}CoCrFeNiSi alloy had better overall corrosion resistance than stainless steel, but its passivation area was also smaller. As mentioned earlier, the addition of Mo plays a beneficial role in building corrosion resistance. In study [53], the addition of Mo to the Co_{1.5}CrFeNi_{1.5}Ti_{0.5}Mo_x alloy proved beneficial, as it significantly increases the pitting potential. Of course, the corrosive environment for HEA alloy applications is also important. Thus, the Co_{1.5}CrFeNi_{1.5}Ti_{0.5}Mo_{0.1} alloy exhibits a wide passivation range in a neutral NaCl corrosive environment and is not susceptible to pitting, but the addition of Mo to the Co-Cr-Fe-Ni-Ti alloy had an adverse effect on corrosion resistance in acidic solutions [53,54]. This effect is related to the formation of a σ phase rich in (Cr, Mo), which in turn reduces the Cr concentration in other phases [53]. However, studies conducted by Shang et al. [31] did not indicate a simple trend in corrosion behavior associated with different Mo_x contents (x = $0.1 \div 0.5$). Improved corrosion resistance was obtained for samples containing Mo0.2 and Mo0.4. The synergistic effect of factors related to the microstructure of HEA alloys and the optimal proportion of Mo and the σ phase was indicated as the reason for the favorable test results.

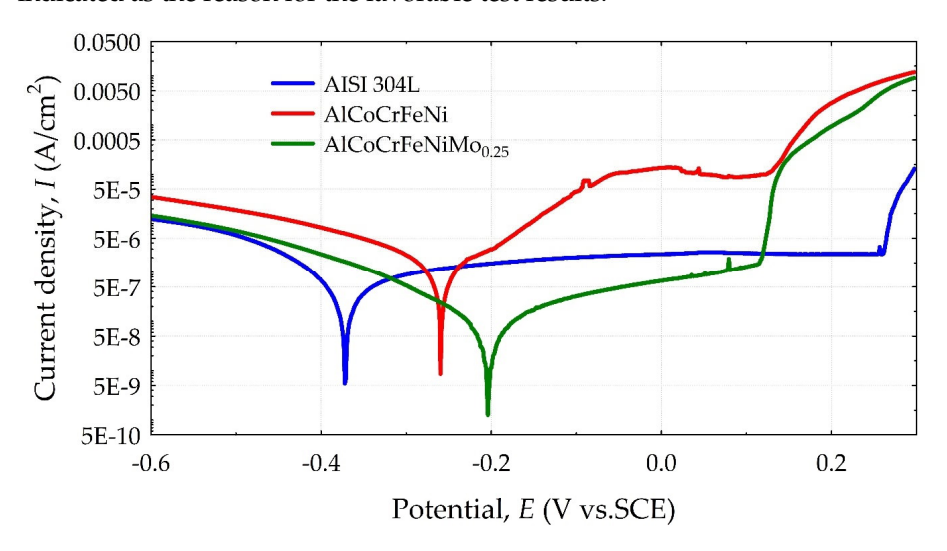


Figure 5. Potentiodynamic polarization curves of tested materials in a 3.5% NaCl solution.

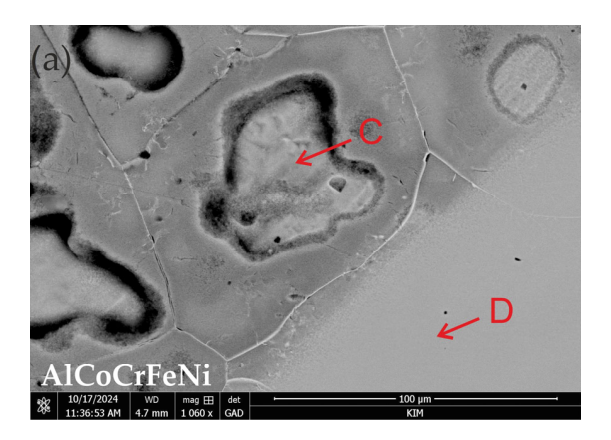
	Table 8. Electrochemical	parameters fo	or the tested	specimens.
--	---------------------------------	---------------	---------------	------------

	i _{corr}	E _{corr}	E _{pit}	CR
Sample No.	[μA·cm ⁻²]	[mV]	[mV]	$ imes 10^{-3}$ [mm·Year ⁻¹]
AISI 304L	0.74 ± 0.04	-352 ± 13	255 ± 17	7.75 ± 0.42
AlCoCrFeNi	2.31 ± 0.06	-252 ± 19	159 ± 10	19.68 ± 0.51
AlCoCrFeNiMo _{0.25}	0.18 ± 0.03	-202 ± 2	128 ± 22	1.52 ± 0.25

Figure 6 presents SEM images of the surfaces after HEA corrosion tests, and the results of local EDS analysis are given in Table 9. In the case of the AlCoCrFeNi alloy (Figure 6a), pitting develops inside the grains. Table 4 (spot B) indicates that the grain boundaries are rich in Cr. Therefore, in this case, corrosion occurs due to Cr segregation, where Cr-depleted grain interiors are predisposed to the formation of corrosion pits. Quantitative EDS analysis (Table 9) shows that Al and, to a lesser extent, Ni corrode inside the grains, as a decrease in the concentration of these two elements is mainly observed in comparison with the results obtained before the corrosion tests (see Table 4). Therefore, areas rich in Al and Ni act as the anode, while areas rich in Cr act as the cathode. The reports by Shi et al. [17] also indicate

Materials 2025, 18, 4566 15 of 22

that in AlxCoCrFeNi alloys (x = 0.5 and 0.7), corrosion pits nucleate in areas rich in Al and Ni of the BCC phase, which is more susceptible to Cl $^-$ ion attack than the FCC phase. In turn, analysis of the mosaic structure of AlCoCrFeNiMo_{0.25} occupied by pits (Figure 6b) indicates that pits develop at the boundaries of areas enriched in Cr and Mo, leading to galvanic corrosion with the adjacent matrix. In this case, EDS analysis (Table 9) clearly indicates a decrease in Al and Ni content in the pitting areas with relatively high Cr and Mo readings. Han et al. [55] point out that Cr-enriched areas representing the σ phase may promote galvanic corrosion at the σ -matrix boundary. On the other hand, areas of material not affected by corrosion pits, occurring in the form of so-called "islands" (Figure 6b, see spot D), may suggest a situation associated with the favorable formation of molybdenum oxide in the passive layer dominated by Cr₂O₃, given the locally high Mo and O content.



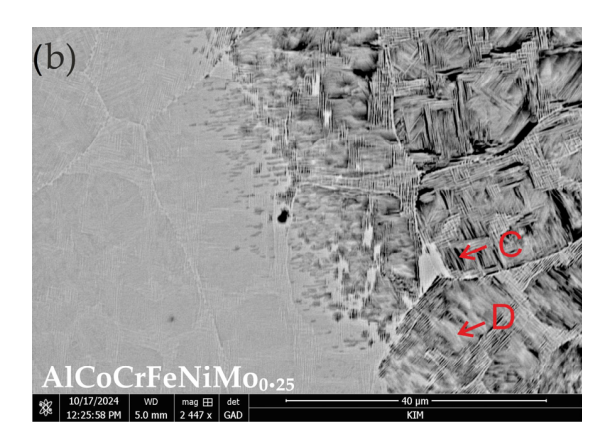


Figure 6. SEM microstructures with points (C and D) of EDS analyses of the surface after corrosion test in 3.5% NaCl solution: (a) AlCoCrFeNi; (b) AlCoCrFeNiMo_{0.25}.

Table 9. EDS analyses for chemical compositions (at. %) of HEA materials after corrosion test.

Sample	Spot	Al	Co	Cr	Fe	Ni	Mo	О
AIC CENT	С	16.47	19.36	18.19	19.31	19.66	_	7.00
AlCoCrFeNi	D	21.02	23.20	18.28	19.42	19.86	_	1.95
A1CaCaEaNiMa	С	0.83	19.54	29.87	22.94	13.07	10.00	3.74
AlCoCrFeNiMo _{0.25}	D	6.04	16.94	22.61	19.34	13.45	12.27	9.35

In order to better visualize the corrosion areas and the role of elements in the corrosion behavior of the tested alloys, Figure 7 presents the EDS analysis in the form of element distribution maps. Pitting corrosion is one of the most common corrosion processes in AISI 304L steel when passive layers are destroyed under the influence of concentrated chloride. The literature data [56,57] indicate that the protective properties of the passive layer of stainless steels are mainly determined by Cr₂O₃, but the following iron oxides may also be present: Fe₂O₃, FeO, and Fe₃O₄. In this case, increased presence of Cr, O, and Fe elements is evident in the immediate vicinity of the pitting. Manganese is generally considered an austenitic element and is added to increase nitrogen solubility [58]. However, its addition is usually accompanied by a reduction in resistance to pitting corrosion, associated with the formation of manganese sulfide (MnS) inclusions, which may constitute pitting initiation sites [3]; small amounts of these were observed as a light blue area on EDS mapping images (Figure 7a). In the case of reference HEA alloys, Cr₂O₃ and Fe₂O₃ oxides have the largest share in the passive layer, which we associate with the most intense decomposition of these elements at the site of corrosion attack (Figure 7b). The element distribution maps reveal that the areas occupied by Ni and, in particular, Al is subject to corrosion. Wang et al. [59] indicate that Al in passive layers is not stable in the presence of Cl⁻. Therefore, Materials 2025, 18, 4566 16 of 22

the protection provided by the oxide layer on alloys with a higher Al content is inferior to that on alloys with a lower Al content. Also, Kao et al. [19], investigating the corrosion resistance of $Al_xCoCrFeNi$ alloys (x = 0, 0.25, 0.5, and 1), found that the protection of the oxide layer on alloys with a higher Al content is worse than on alloys with a lower Al content, because despite the easy formation of a thicker oxide layer, it is porous. The reason for the poorer protective quality of the passive layer is the decrease in the proportion of Cr_2O_3 with an increase in Al content. Shi et al. [60] demonstrated that as the Al content in the $Al_xCoCrFeNi$ alloy increases, the Cr^{3+} and $Fe^{2+,3+}$ contents decreases. This is because the passive layer containing more Al oxides and hydroxides is thicker but less protective and susceptible to attack by aggressive Cl^- ions. It is worth noting that hydroxides in the passive layer have been shown to have a lower density than oxides [61].

Similarly, in the case of the AlCoCrFeNiMo_{0.25} alloy (Figure 7c), a lower presence of Al and Ni is observed in areas where pitting occurs, confirming the susceptibility of these elements to corrosion. In contrast, higher concentrations of O, Cr, and Mo are observed in these areas. Dai et al. [29] have proven that the addition of Mo may slightly thicken the passive layer, improving the protective properties of HEA alloys with Mo in a highly aggressive Cl⁻ environment by modifying the composition and thickness of the passive layer, which is a result of increasing the Cr₂O₃/Cr(OH)₃ ratio and incorporating Mo oxides into the passive layer. With higher amounts of Mo0.2 and Mo0.25 in AlCoCrFeNiMo_x alloys, a (Cr, Mo)-rich σ phase appears, acting as a cathode and consequently causing local galvanic corrosion [5]. Galvanic corrosion for $CoCrFeNiMo_x$ (x = 0.3–0.5), which occurred at dendrite junctions and at interfaces around the σ phase, was also caused by element segregation with a small anode/cathode interaction area [31]. The obtained oxidation state of Co, Cr, Fe, Ni, and Mo in the passive layer of CoCrFeNiMo_x alloys was in the form of Co²⁺, Cr³⁺, Fe³⁺, Ni²⁺, Mo⁴⁺, and Mo⁶⁺. Furthermore, it was demonstrated that the oxidation state of elements such as Cr, Fe, and Mo played a leading role compared to their metallic state, while Co and Ni were mainly present in their metallic state. Interestingly, the authors of the study [31] suggested that in the case of Mo, it is Mo⁶⁺ that plays the main role in delaying corrosion, and not Mo⁴⁺.

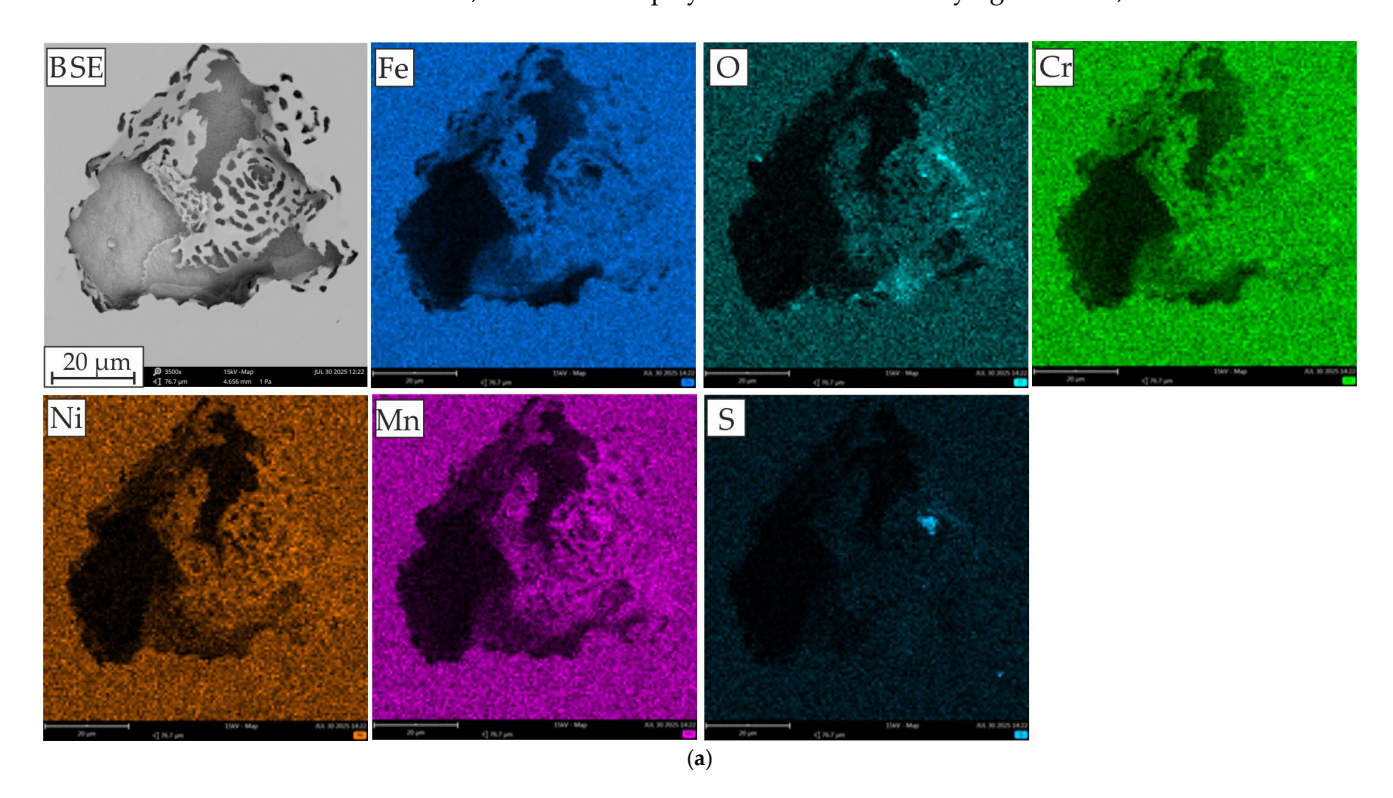


Figure 7. Cont.

Materials **2025**, 18, 4566 17 of 22

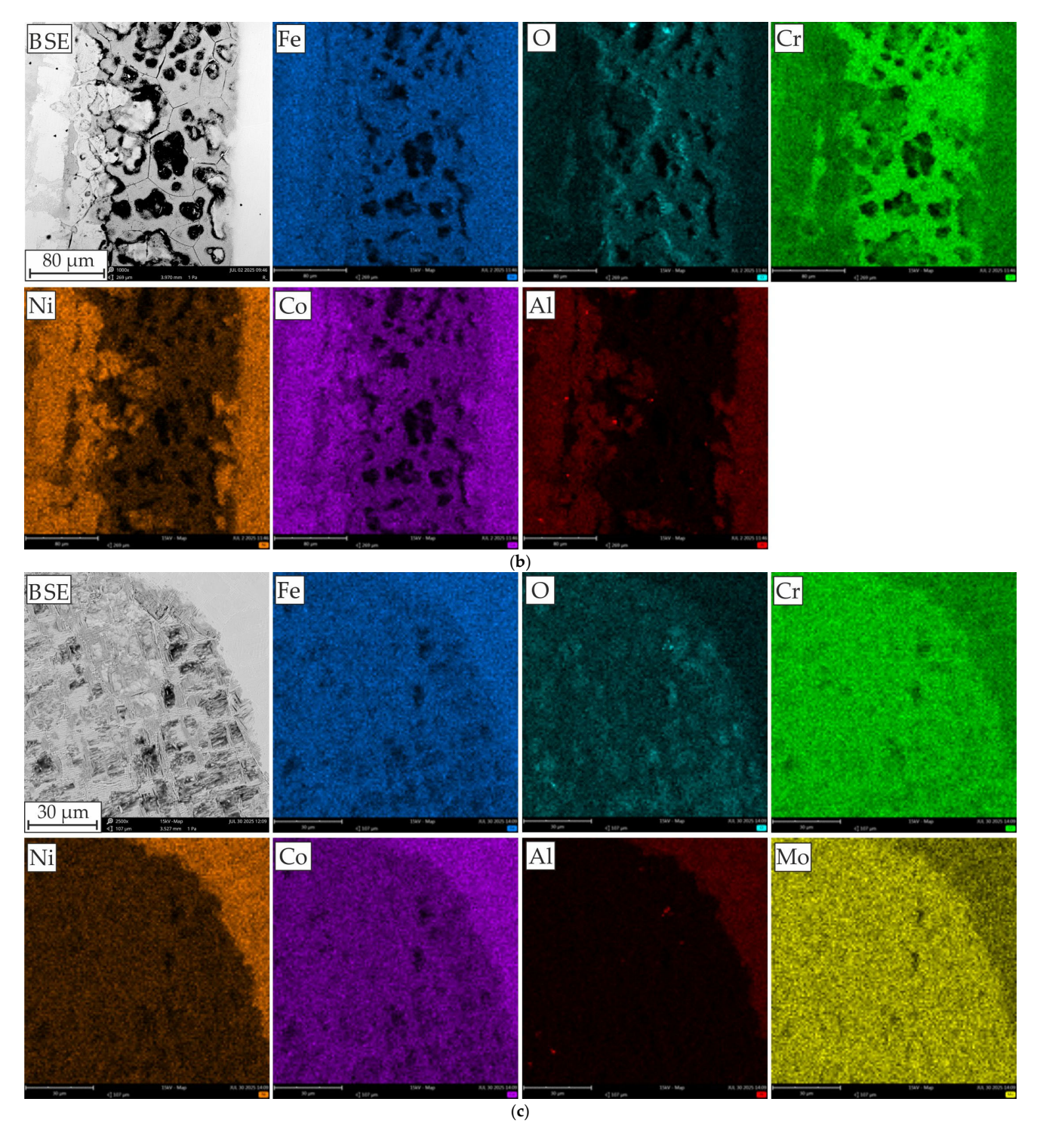


Figure 7. SEM-BSE and EDS mapping images of: (a) AISI 304L, (b) AlCoCrFeNi, and (c) AlCoCrFeNi $Mo_{0.25}$.

Based on corrosion tests and SEM-EDS analyses of surfaces after corrosion tests in 3.5% NaCl, a diagram of the corrosion mechanism of the tested HEA alloys was prepared (Figure 8). In the case of equiatomic HEA alloy, the (Al, Ni)-rich BCC phase depleted in Cr, which acts as the anode, undergoes local corrosion, which can be compared to the corrosion phenomena occurring in stainless steels (Figure 8a,c). Then, a passive film dominated by Cr_2O_3 forms on the cathode surface (at the grain boundaries rich in Cr). As demonstrated by Nie et al. [62], Cr_2O_{33} is denser and has better protective properties for the matrix

Materials 2025, 18, 4566 18 of 22

than Al_2O_3 . However, it should be considered that the surface of the alloy has a larger proportion of areas constituting the anode, which translates into a higher proportion of Al_2O_3 . As a result, the protective properties of the interior of the grains (constituting the matrix) deteriorate as the time spent in the electrolyte solution increases. In turn, in the case of the $AlCoCrFeNiMo_{0.25}$ alloy with a mosaic structure (Figure 8b), there is a potential difference between the phase rich in Cr and Mo precipitates (forming the cathode) and the phase rich in Al and Ni (acting as a microanode—represented in gray). Therefore, areas rich in Al and Ni will be preferentially corroded as a result of the galvanic microcorrosion (Figure 8d). As the lamellar phase constituting the anode undergoes further dissolution, a passive film (rich in Cr_2O_3 and MoO_4) forms between the lamellar areas rich in Cr and Mo. Due to the mosaic structure of the $AlCoCrFeNiMo_{0.25}$ alloy, the anode and cathode areas are balanced, resulting in significantly better corrosion resistance compared to the equiatomic HEA alloy.

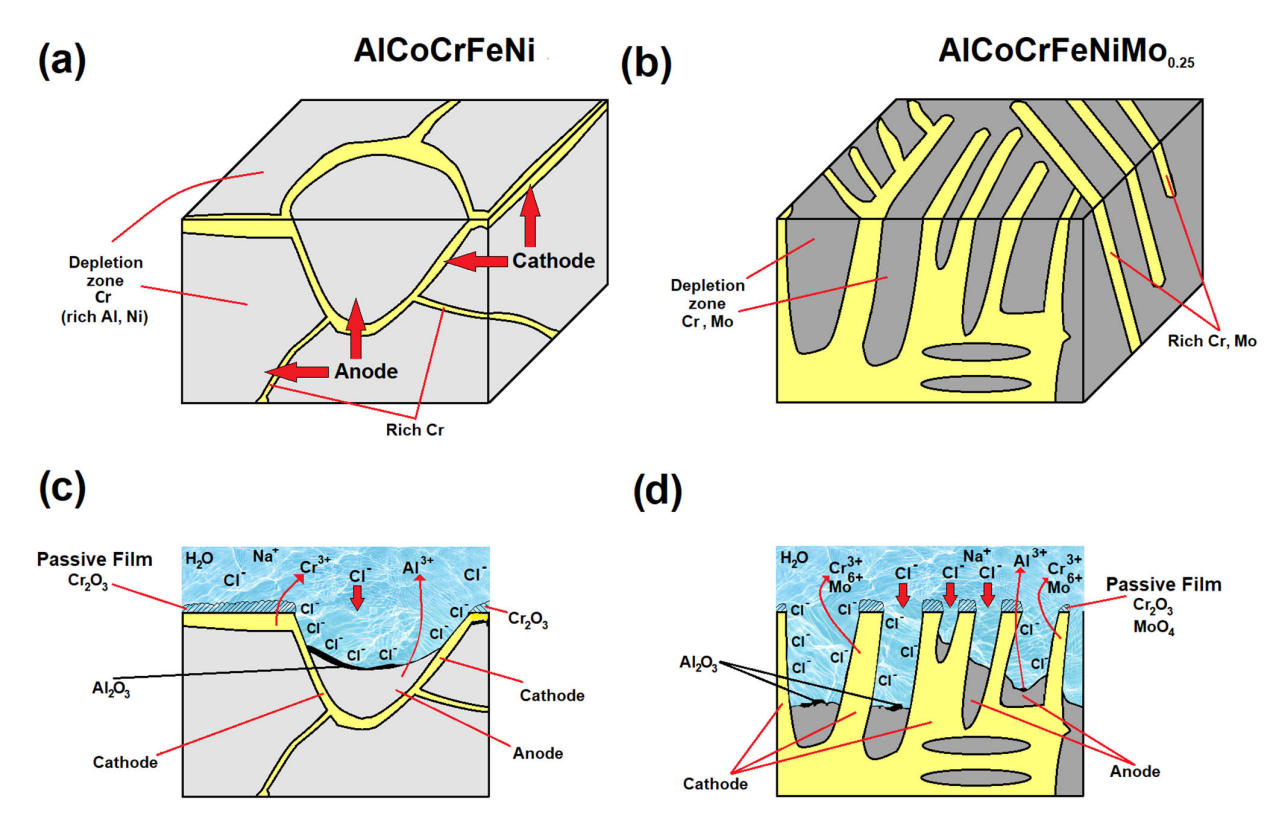


Figure 8. Schematic diagram for corrosion mechanism of AlCoCrFeNi and AlCoCrFeNiMo_{0.25}: (a,b) galvanic corrosion, (c) corrosion of the equiatomic HEA, and (d) corrosion of the mosaic structure.

4. Conclusions

In general, the addition of the element at a level of Mo0.25 significantly affects the microstructure, mechanical properties, and corrosion resistance of the AlCoCrFeNiMo $_{\rm X}$ alloy. Based on the research conducted, it was found that:

- The addition of Mo creates a mosaic-patterned microstructure, and XRD analysis indicated the presence of the σ phase, whereby the XRD analysis showed that the average grain sizes for B2/BCC phases have a smaller size after Mo addition.
- Based on Vickers hardness tests, the surface of the HEA alloy with Mo showed a more than 3-fold-increase in hardness compared to AISI 304L, with an increase of nearly 50% compared to the reference HEA, which can be attributed to lattice distortion by Mo, grain refinement, and the presence of a hard and brittle σ phase.

Materials 2025, 18, 4566

• Nanoidentification tests have shown that the addition of Mo increases hardness (H) and elastic modulus (E) and improves the H/E and H^3/E^2 ratios, also causing an increase in the elastic recovery index with a decreasing plasticity index. This indicates an improvement in anti-wear properties with resistance to impact loading.

- Polarization tests in 3.5% NaCl showed that the addition of Mo improves the corrosion resistance of HEA alloys, manifested by a decrease in corrosion current density and, thus, a decrease in corrosion rate and a shift in the corrosion potential towards higher values.
- EIS corrosion tests showed that the phase angle and impedance modulus values for AlCoCrFeNiMo_{0.25} were higher in the low-frequency range, indicating the formation of a more stable passive layer. Furthermore, in the low-frequency range, all tested surfaces were characterized by high impedance above $10^5~\Omega \cdot \text{cm}^2$, indicating that these surfaces have adequate corrosion resistance in a 0.9% NaCl solution, making them suitable for medical applications in this respect. All tested materials behaved almost like an ideal capacitor.
- SEM-EDS analysis of the surface after the corrosion tests revealed that in the case of the AlCoCrMFeNi equivalent alloy, corrosion occurs due to Cr segregation, where the Cr-depleted grain interiors are predisposed to the formation of corrosion pits, and the Al- and Ni-rich grain interiors are subject to corrosion. Areas rich in Al and Ni form the anode, while areas rich in Cr form the cathode. In the case of HEA with Mo, pits developed at the boundaries of areas enriched in Cr and Mo, leading to galvanic corrosion with an adjacent matrix (rich in Al and Ni).

Author Contributions: Conceptualization, M.W. and W.J.N.; methodology, M.W. and D.C.; software, M.W.; validation, M.W.; formal analysis, M.W.; investigation, M.W., W.O., D.C. and W.J.N.; resources, M.W.; data curation, M.W. and W.O.; writing—original draft preparation, M.W. and D.C.; writing—review and editing, M.W., W.J.N. and W.O.; visualization, M.W.; supervision, M.W.; project administration, M.W. and W.O.; funding acquisition, M.W. All authors have read and agreed to the published version of the manuscript.

Funding: The APC publication fee was fully covered by the authors' voucher. Author Voucher discount code (7cecd4aae5117633).

Institutional Review Board Statement: Not applicable.

Informed Consent Statement: Not applicable.

Data Availability Statement: The raw data supporting the conclusions of this article will be made available by the authors on request.

Acknowledgments: The research leading to these results has received funding from the commissioned task entitled "VIA CARPATIA Universities of Technology Network named after the President of the Republic of Poland Lech Kaczyński" under the special purpose grant from the Minister of Education and Science, contract no. MEiN/2022/DPI/2575, as part of the action "In the Neighborhood—Interuniversity Research Internships and Study Visits".

Conflicts of Interest: The authors declare no conflicts of interest.

References

- 1. Krella, A.K.; Zakrzewska, D.E.; Buszko, M.H.; Marchewicz, A. Effect of Thermal Treatment and Erosion Aggressiveness on Resistance of S235JR Steel to Cavitation and Slurry. *Materials* **2021**, *14*, 1456. [CrossRef]
- 2. Nair, R.B.; Arora, H.S.; Boyana, A.V.; Saiteja, P.; Grewal, H.S. Tribological Behavior of Microwave Synthesized High Entropy Alloy Claddings. *Wear* **2019**, 436–437, 203028. [CrossRef]
- 3. Pardo, A.; Merino, M.C.; Coy, A.E.; Viejo, F.; Arrabal, R.; Matykina, E. Pitting Corrosion Behaviour of Austenitic Stainless Steels—Combining Effects of Mn and Mo Additions. *Corros. Sci.* **2008**, *50*, 1796–1806. [CrossRef]

Materials 2025, 18, 4566 20 of 22

4. Chen, Y.Y.; Duval, T.; Hung, U.D.; Yeh, J.W.; Shih, H.C. Microstructure and Electrochemical Properties of High Entropy Alloys—A Comparison with Type-304 Stainless Steel. *Corros. Sci.* **2005**, *47*, 2257–2279. [CrossRef]

- 5. Walczak, M.; Nowak, W.J.; Szala, M.; Grądzka-Dahlke, M.; Maciaszek, N.; Vališ, D.; Pasierbiewicz, K. Effect of Molybdenum Addition on Microstructure and Behavior of AlCoCrFeNi High-Entropy Alloys in Wet Environments. *Arch. Civ. Mech. Eng.* **2025**, 25, 205. [CrossRef]
- 6. Tsai, M.-H.; Yeh, J.-W. High-Entropy Alloys: A Critical Review. Mater. Res. Lett. 2014, 2, 107–123. [CrossRef]
- 7. Arif, Z.U.; Khalid, M.Y.; Ur Rehman, E.; Ullah, S.; Atif, M.; Tariq, A. A Review on Laser Cladding of High-Entropy Alloys, Their Recent Trends and Potential Applications. *J. Manuf. Process.* **2021**, *68*, 225–273. [CrossRef]
- 8. Yeh, J.-W.; Chen, S.-K.; Lin, S.-J.; Gan, J.-Y.; Chin, T.-S.; Shun, T.-T.; Tsau, C.-H.; Chang, S.-Y. Nanostructured High—Entropy Alloys with Multiple Principal Elements: Novel Alloy Design Concepts and Outcomes. *Adv. Eng. Mater.* **2004**, *6*, 299–303. [CrossRef]
- 9. Wang, F.J.; Zhang, Y.; Chen, G.L.; Davies, H.A. Cooling Rate and Size Effect on the Microstructure and Mechanical Properties of AlCoCrFeNi High Entropy Alloy. *J. Eng. Mater. Technol.* **2009**, *131*, 034501. [CrossRef]
- 10. Cheng, K.-C.; Chen, J.-H.; Stadler, S.; Chen, S.-H. Properties of Atomized AlCoCrFeNi High-Entropy Alloy Powders and Their Phase-Adjustable Coatings Prepared via Plasma Spray Process. *Appl. Surf. Sci.* **2019**, *478*, 478–486. [CrossRef]
- Joseph, J.; Jarvis, T.; Wu, X.; Stanford, N.; Hodgson, P.; Fabijanic, D.M. Comparative Study of the Microstructures and Mechanical Properties of Direct Laser Fabricated and Arc-Melted Al_xCoCrFeNi High Entropy Alloys. *Mater. Sci. Eng. A* 2015, 633, 184–193.
 [CrossRef]
- 12. Kao, Y.-F.; Chen, T.-J.; Chen, S.-K.; Yeh, J.-W. Microstructure and Mechanical Property of As-Cast, -Homogenized, and -Deformed Al_x CoCrFeNi (0 \leq x \leq 2) High-Entropy Alloys. *J. Alloys Compd.* **2009**, 488, 57–64. [CrossRef]
- 13. Tokarewicz, M.; Grądzka-Dahlke, M. Review of Recent Research on AlCoCrFeNi High-Entropy Alloy. *Metals* **2021**, *11*, 1302. [CrossRef]
- Wang, F.J.; Zhang, Y.; Chen, G.L. Atomic Packing Efficiency and Phase Transition in a High Entropy Alloy. J. Alloys Compd. 2009, 478, 321–324. [CrossRef]
- 15. Ogura, M.; Fukushima, T.; Zeller, R.; Dederichs, P.H. Structure of the High-Entropy Alloy Al CrFeCoNi: Fcc versus Bcc. *J. Alloys Compd.* **2017**, 715, 454–459. [CrossRef]
- 16. Tang, Z.; Gao, M.C.; Diao, H.; Yang, T.; Liu, J.; Zuo, T.; Zhang, Y.; Lu, Z.; Cheng, Y.; Zhang, Y.; et al. Aluminum Alloying Effects on Lattice Types, Microstructures, and Mechanical Behavior of High-Entropy Alloys Systems. *JOM* **2013**, *65*, 1848–1858. [CrossRef]
- 17. Shi, Y.; Yang, B.; Xie, X.; Brechtl, J.; Dahmen, K.A.; Liaw, P.K. Corrosion of Al CoCrFeNi High-Entropy Alloys: Al-Content and Potential Scan-Rate Dependent Pitting Behavior. *Corros. Sci.* **2017**, *119*, 33–45. [CrossRef]
- 18. Lin, C.-M.; Tsai, H.-L. Evolution of Microstructure, Hardness, and Corrosion Properties of High-Entropy Al_{0.5}CoCrFeNi Alloy. *Intermetallics* **2011**, *19*, 288–294. [CrossRef]
- 19. Kao, Y.-F.; Lee, T.-D.; Chen, S.-K.; Chang, Y.-S. Electrochemical Passive Properties of Al_xCoCrFeNi (x = 0, 0.25, 0.50, 1.00) Alloys in Sulfuric Acids. *Corros. Sci.* **2010**, 52, 1026–1034. [CrossRef]
- 20. Liu, H.; Sun, S.; Zhang, T.; Zhang, G.; Yang, H.; Hao, J. Effect of Si Addition on Microstructure and Wear Behavior of AlCoCrFeNi High-Entropy Alloy Coatings Prepared by Laser Cladding. *Surf. Coat. Technol.* **2021**, 405, 126522. [CrossRef]
- Ma, S.G.; Zhang, Y. Effect of Nb Addition on the Microstructure and Properties of AlCoCrFeNi High-Entropy Alloy. *Mater. Sci. Eng. A* 2012, 532, 480–486. [CrossRef]
- 22. Tokarewicz, M.; Gradzka-Dahlke, M.; Nowak, W.J.; Gradzik, A.; Szala, M.; Walczak, M. Effect of Vanadium Addition on the Wear Resistance of Al_{0.7}CoCrFeNi High-Entropy Alloy. *Materials* **2024**, *17*, 6021. [CrossRef] [PubMed]
- 23. Chen, Q.; Dong, Y.; Zhang, J.; Lu, Y. Microstructure and Properties of AlCoCrFeNiB_x(x = 0, 0.1, 0.25, 0.5, 0.75, 1.0) High Entropy Alloys. *Rare Met. Mater. Eng.* **2017**, *46*, 651–656. [CrossRef]
- 24. Chen, J.; Niu, P.; Liu, Y.; Lu, Y.; Wang, X.; Peng, Y.; Liu, J. Effect of Zr Content on Microstructure and Mechanical Properties of AlCoCrFeNi High Entropy Alloy. *Mater. Des.* **2016**, *94*, 39–44. [CrossRef]
- 25. Hassan, M.A.; Yehia, H.M.; Mohamed, A.S.A.; El-Nikhaily, A.E.; Elkady, O.A. Effect of Copper Addition on the AlCoCrFeNi High Entropy Alloys Properties via the Electroless Plating and Powder Metallurgy Technique. *Crystals* **2021**, *11*, 540. [CrossRef]
- 26. Nowak, W.J.; Kubaszek, T.; Gradzik, A.; Grądzka-Dahlke, M.; Perkowski, D.; Tokarewicz, M.; Walczak, M.; Szala, M. Effect of Ti Doping of Al_{0.7}CoCrFeNi-Based High Entropy Alloys on Their Erosion Resistance by Solid Particles. *Materials* **2025**, *18*, 3328. [CrossRef]
- 27. Zhang, D.; Li, Q.; Sun, R.; Chang, C.; Liu, B.; Ma, X. Effect of Mn Addition on Microstructure and Corrosion Behavior of AlCoCrFeNi High-Entropy Alloy. *Intermetallics* **2024**, *167*, 108236. [CrossRef]
- 28. Zhu, J.M.; Fu, H.M.; Zhang, H.F.; Wang, A.M.; Li, H.; Hu, Z.Q. Microstructures and Compressive Properties of Multicomponent AlCoCrFeNiMo_x Alloys. *Mater. Sci. Eng. A* **2010**, 527, 6975–6979. [CrossRef]
- 29. Dai, C.; Zhao, T.; Du, C.; Liu, Z.; Zhang, D. Effect of Molybdenum Content on the Microstructure and Corrosion Behavior of FeCoCrNiMo_x High-Entropy Alloys. *J. Mater. Sci. Technol.* **2020**, *46*, 64–73. [CrossRef]

Materials 2025, 18, 4566 21 of 22

30. Zhuang, Y.X.; Zhang, X.L.; Gu, X.Y. Effect of Molybdenum on Phases, Microstructure and Mechanical Properties of Al_{0.5}CoCrFeMo Ni High Entropy Alloys. *J. Alloys Compd.* **2018**, 743, 514–522. [CrossRef]

- 31. Shang, X.-L.; Wang, Z.-J.; Wu, Q.-F.; Wang, J.-C.; Li, J.-J.; Yu, J.-K. Effect of Mo Addition on Corrosion Behavior of High-Entropy Alloys CoCrFeNiMo_x in Aqueous Environments. *Acta Metall. Sin. (Engl. Lett.)* **2019**, *32*, 41–51. [CrossRef]
- 32. Oliver, W.C.; Pharr, G.M. Measurement of Hardness and Elastic Modulus by Instrumented Indentation: Advances in Understanding and Refinements to Methodology. *J. Mater. Res.* **2004**, *19*, 3–20. [CrossRef]
- 33. *PN-EN ISO* 14577-1:2015; Metallic Materials—Instrumented Indentation Test for Hardness and Materials Parameters—Part 1: Test Method. ISO: Geneva, Switzerland, 2015.
- 34. *ASTM Standard G* 102–89; Standard Practice for Calculation of Corrosion Rates and Related Information from Electrochemical Measurements. ASTM International: West Conshohocken, PA, USA, 2004.
- 35. Shi, X.; Wang, C.; Huang, M.; Cui, H. Microstructure and Wear Resistance Property of AlFeCrNiMo_x Coatings by Plasma Cladding. *Mater. Res. Express* **2019**, *6*, 106537. [CrossRef]
- 36. Nowak, W.J.; Jopek, J.; Maciaszek, N. Effect of Mo Addition on the Oxidation Behavior of the AlCoCrFeNi High Entropy Alloy. *Adv. Sci. Technol. Res. J.* 2026; 20, *in press*.
- 37. Xu, W.; Salas, D.; Sahu, B.; Xiang, S.; Skokan, M.; Butler, B.; Arroyave, R.; Karaman, I. Enhanced Strain Hardening Response of Multi-Principal Element Alloys with L12 Nanodomains Designed for Multiple Objectives and Constraints. *Mater. Today Commun.* 2025, 48, 113265. [CrossRef]
- 38. Xi, R.; Li, Y. Recent Advances in the Performance and Mechanisms of High-Entropy Alloys Under Low- and High-Temperature Conditions. *Coatings* **2025**, *15*, 92. [CrossRef]
- 39. Chudoba, T.; Richter, F. Investigation of Creep Behaviour under Load during Indentation Experiments and Its Influence on Hardness and Modulus Results. *Surf. Coat. Technol.* **2001**, *148*, 191–198. [CrossRef]
- 40. Tian, L.; Jiao, Z.M.; Yuan, G.Z.; Ma, S.G.; Wang, Z.H.; Yang, H.J.; Zhang, Y.; Qiao, J.W. Effect of Strain Rate on Deformation Behavior of AlCoCrFeNi High-Entropy Alloy by Nanoindentation. *J. Mater. Eng. Perform.* **2016**, *25*, 2255–2260. [CrossRef]
- 41. Jiao, Z.-M.; Ma, S.-G.; Yuan, G.-Z.; Wang, Z.-H.; Yang, H.-J.; Qiao, J.-W. Plastic Deformation of Al_{0.3}CoCrFeNi and AlCoCrFeNi High-Entropy Alloys Under Nanoindentation. *J. Mater. Eng. Perform.* **2015**, 24, 3077–3083. [CrossRef]
- 42. Okoro, A.M.; Lephuthing, S.S.; Rasiwela, L.; Olubambi, P.A. Nondestructive Measurement of the Mechanical Properties of Graphene Nanoplatelets Reinforced Nickel Aluminium Bronze Composites. *Heliyon* **2021**, 7, e07978. [CrossRef]
- 43. Oyen, M.L.; Cook, R.F. A Practical Guide for Analysis of Nanoindentation Data. *J. Mech. Behav. Biomed. Mater.* **2009**, 2, 396–407. [CrossRef] [PubMed]
- 44. Szala, M.; Walczak, M.; Pasierbiewicz, K.; Kamiński, M. Cavitation Erosion and Sliding Wear Mechanisms of AlTiN and TiAlN Films Deposited on Stainless Steel Substrate. *Coatings* **2019**, *9*, 340. [CrossRef]
- 45. Walczak, M.; Pasierbiewicz, K.; Szala, M. Effect of Ti6Al4V Substrate Manufacturing Technology on the Properties of PVD Nitride Coatings. *Acta Phys. Pol. A* **2022**, 142, 723–732. [CrossRef]
- 46. Yan, C.; Bor, B.; Plunkett, A.; Domènech, B.; Schneider, G.A.; Giuntini, D. Nanoindentation of Supercrystalline Nanocomposites: Linear Relationship Between Elastic Modulus and Hardness. *JOM* **2022**, 74, 2261–2276. [CrossRef]
- 47. Ayyagari, A.; Barthelemy, C.; Gwalani, B.; Banerjee, R.; Scharf, T.W.; Mukherjee, S. Reciprocating Sliding Wear Behavior of High Entropy Alloys in Dry and Marine Environments. *Mater. Chem. Phys.* **2018**, 210, 162–169. [CrossRef]
- 48. Orazem, M.E.; Tribollet, B. A Tutorial on Electrochemical Impedance Spectroscopy. ChemTexts 2020, 6, 12. [CrossRef]
- 49. Walczak, M.; Okuniewski, W.; Nowak, W.J.; Chocyk, D.; Pasierbiewicz, K. Corrosion Behavior of Shot Peened Ti6Al4V Alloy Fabricated by Conventional and Additive Manufacturing. *Materials* **2025**, *18*, 2274. [CrossRef]
- 50. Żebrowski, R.; Walczak, M. The Effect of Shot Peening on the Corrosion Behaviour of Ti-6Al-4V Alloy Made by DMLS. *Adv. Mater. Sci.* **2018**, *18*, 43–54. [CrossRef]
- 51. Meghwal, A.; Anupam, A.; Luzin, V.; Schulz, C.; Hall, C.; Murty, B.S.; Kottada, R.S.; Berndt, C.C.; Ang, A.S.M. Multiscale Mechanical Performance and Corrosion Behaviour of Plasma Sprayed AlCoCrFeNi High-Entropy Alloy Coatings. *J. Alloys Compd.* **2021**, 854, 157140. [CrossRef]
- 52. Lee, C.P.; Chang, C.C.; Chen, Y.Y.; Yeh, J.W.; Shih, H.C. Effect of the Aluminium Content of Al_xCrFe_{1.5}MnNi_{0.5} High-Entropy Alloys on the Corrosion Behaviour in Aqueous Environments. *Corros. Sci.* **2008**, *50*, 2053–2060. [CrossRef]
- 53. Chou, Y.L.; Yeh, J.W.; Shih, H.C. Effect of Molybdenum on the Pitting Resistance of Co_{1.5}CrFeNi_{1.5}Ti_{0.5}Mo_x Alloys in Chloride Solutions. *Corrosion* **2011**, *67*, 085002–1–085002–6. [CrossRef]
- 54. Chou, Y.L.; Yeh, J.W.; Shih, H.C. The Effect of Molybdenum on the Corrosion Behaviour of the High-Entropy Alloys Co_{1.5}CrFeNi_{1.5}Ti_{0.5}Mo_x in Aqueous Environments. *Corros. Sci.* **2010**, *52*, 2571–2581. [CrossRef]
- 55. Han, Z.; Ren, W.; Yang, J.; Tian, A.; Du, Y.; Liu, G.; Wei, R.; Zhang, G.; Chen, Y. The Corrosion Behavior of Ultra-Fine Grained CoNiFeCrMn High-Entropy Alloys. *J. Alloys Compd.* **2020**, *816*, 152583. [CrossRef]
- 56. Boudalia, M.; Guenbour, A.; Bellaouchou, A.; Fernandez-Domene, R.M.; Garcia-Anton, J. Corrosion Behaviour of a Highly Alloyed Austenitic Alloy UB6 in Contaminated Phosphoric Acid. *Int. J. Corros.* **2013**, 2013, 363826. [CrossRef]

Materials 2025, 18, 4566 22 of 22

57. Radojković, B.; Jegdić, B.; Pejić, J.; Eraković Pantović, S.; Marunkić, D.; Simović, A.; Milošević, M.; Alić, B. Passive Film Properties and Corrosion Resistance of AISI 304L Stainless Steel. *Corros. Eng. Sci. Technol. Int. J. Corros. Process. Corros. Control* 2025, 60, 233–249. [CrossRef]

- 58. *Stainless Steels*; Davis, J.R., Ed.; ASM Specialty Handbook; ASM International: Materials Park, OH, USA, 1994; ISBN 978-0-87170-503-7.
- 59. Wang, K.; Lan, A.D.; Qiao, J.W. Corrosion Behavior of Al0.1CoCrFeNi High Entropy Alloy in Various Chloride-Containing Solutions. *Front. Mater.* **2021**, *7*, 533843. [CrossRef]
- 60. Shi, Y.; Collins, L.; Balke, N.; Liaw, P.K.; Yang, B. In-Situ Electrochemical-AFM Study of Localized Corrosion of Al CoCrFeNi High-Entropy Alloys in Chloride Solution. *Appl. Surf. Sci.* **2018**, 439, 533–544. [CrossRef]
- 61. Vargel, C. Introducton to The Corrosion of Aluminium. In *Corrosion of Aluminium*; Elsevier: Amsterdam, The Netherlands, 2004; pp. 81–109, ISBN 978-0-08-044495-6.
- 62. Nie, S.; Zheng, Z.; Qiao, Y.; Duan, Y.; Cui, J.; Mekkey, S.D.; Amin, M.A.; Melhi, S.; Yang, H.; Zhou, H.; et al. Corrosion Behavior of As-Cast Al_{0.75}CoCr_{1.25}FeNi High Entropy Alloy in 0.5 mol/L Sulfuric Acid. *Adv. Compos. Hybrid Mater.* **2024**, 7, 138. [CrossRef]

Disclaimer/Publisher's Note: The statements, opinions and data contained in all publications are solely those of the individual author(s) and contributor(s) and not of MDPI and/or the editor(s). MDPI and/or the editor(s) disclaim responsibility for any injury to people or property resulting from any ideas, methods, instructions or products referred to in the content.